3-1-2023

Impact of pressure drop oscillations and parallel channel instabilities on microchannel flow boiling and critical heat flux

M. D. Clark

Justin Weibel
jaweibel@purdue.edu

S. V. Garimella

Clark, M. D.; Weibel, Justin; and Garimella, S. V., "Impact of pressure drop oscillations and parallel channel instabilities on microchannel flow boiling and critical heat flux" (2023). *CTRC Research Publications.* Paper 402.
http://dx.doi.org/https://doi.org/10.1016/j.ijmultiphaseflow.2023.104380

Impact of Pressure Drop Oscillations and Parallel Channel Instabilities on Microchannel Flow Boiling and Critical Heat Flux

Matthew D. Clark, Justin A. Weibel[1], Suresh V. Garimella[2]

Cooling Technologies Research Center, School of Mechanical Engineering

Purdue University, 585 Purdue Mall, West Lafayette, IN 47907 USA

Abstract

Microchannel flow boiling heat sinks that leverage the highly efficient heat transfer mechanisms associated with phase change are a primary candidate for cooling next-generation electronics in electric vehicles. In order to design flow boiling heat sinks for such practical applications, one key obstacle is an understanding of the conditions for occurrence of dynamic two-phase flow instabilities, to which microscale flow boiling is particularly susceptible, as well as their impact on heat transfer performance. While mapping the operational regimes of these instabilities has been well-studied, with numerous stability criteria available, their impact on the heat transfer performance of heat sinks in practical applications is not understood. This work seeks to assess the impact of pressure drop oscillations and parallel channel instabilities on the surface temperature and critical heat flux in parallel microchannel heat sinks. This is achieved through measurement of time-averaged steady-state temperatures and pressures, combined with high-frequency pressure signals and high-speed flow visualization. These data are compared across three controlled flow configurations that comprise a condition of stable flow boiling, a condition where only parallel channel instabilities can occur, and a third where both pressure drop oscillations and parallel channel instabilities can occur. Experiments are performed using the dielectric refrigerant HFE-7100 in 2 cm long parallel microchannel heat sinks with square-cross-section channels (0.25, 0.5, 0.75, and 1 mm widths) at three mass fluxes (100, 400, and 1600 kg/m^{2}s). Across this range of conditions, the time-averaged surface temperature and critical heat flux were remarkably insensitive to the occurrence of these instabilities despite the significant hydrodynamic events and transient flow patterns observed.

Keywords

Flow boiling; instabilities; compressibility; microchannels; two-phase heat transfer; electronics cooling

---

[1] Corresponding author E-mail address: jaweibel@purdue.edu

[2] Suresh Garimella is currently with The University of Vermont, Burlington, VT 05405 USA.

Nomenclature

A_{wet}	total heat sink wetted area [m^2]
Bl	Boiling number ($q"/(Gh_{fg})$)
f	oscillation frequency [Hz]
G	mass flux [kg/m^2s]
h_c	channel height [mm]
h_{fh}	latent heat of vaporization [J/kg]
I	electrical current [A]
N	number of channels
P_{inlet}	pressure measured at test section inlet [kPa]
$\hat{P}_{inlet}$	inlet pressure oscillation about mean value ($P_{inlet} - P_{inlet,mean}$) [kPa]
q''	wetted-area heat flux ($(P_{elec} - Q_{loss})/A_{wet}$) [$W/cm^2$]
Q_{loss}	heat loss [W]
T_s	average extrapolated surface temperature [°C]
T_{sat}	fluid saturation temperature [°C]
P_{elec}	electrical power ($\Delta V*I$) [W]
ΔV	power supply voltage drop [V]
$\dot{V}$	volumetric flow rate [mL/min]
w_c	channel width [mm]
α	thermal diffusivity [m^2/s]
δ_p	thermal penetration depth ($4\sqrt{2\pi\alpha/f}$) [m]

1 Introduction

As technological and physical packaging requirements of next-generation electronic devices continue toward higher power densities, thermal management strategies must be improved over conventional single-phase air or liquid cold plates [1]–[3]. A specific application having challenging thermal management demands is the traction power inverter modules necessary for propulsion of electric vehicles. The most promising methods for meeting the needs of these high-power-density packages utilize the highly efficient heat transfer mechanisms associated with liquid-vapor phase change. At the cutting-edge of heat sink technology, researchers have demonstrated the integration of microfluidic two-phase cooling channels directly into semiconductor devices, achieving heat dissipation in excess of 1000 W/cm^2 [4]–[7]. In applications such as power converter modules in electric vehicles, a nearer-term approach is the operation of conventional or reduced-volume cold plate designs in the two-phase regime. However, in all instances of the practical implementation of pumped two-phase loops, challenges remain. Of these challenges, two-phase flow instabilities have been a subject of concern for many decades in macroscale systems such as nuclear reactors and heat exchangers [8], [9]. These same instabilities are also observed, if not exacerbated, at smaller scales such as in microchannel cold plates [10].

Two-phase flow instabilities are broadly categorized as either static or dynamic [8]. Static instabilities are characterized by a flow which, when disturbed, transitions from one unstable operating condition to a different stable operating condition, such as during the Ledinegg instability [11], [12]. Dynamic instabilities are a result of interactions and delayed feedback between, for example, the inertia of a two-phase mixture within a heated channel and a source of compressibility outside of the channel [9], [13]. In microchannel heat sinks, two types of dynamic instabilities are of particular concern: pressure drop oscillations and parallel channel instabilities. Pressure drop oscillations are a result of the two-phase mixture within the heat sink interacting with a source of compressibility, such as trapped noncondensable gas, upstream of the heat sink. Parallel channel instabilities are dictated by similar system compressibility mechanisms, but instead result from interactions between the two-phase mixtures in neighboring channels within a heat sink, as described in more detail below.

In a channel with constant heating, the pressure required to maintain a given mass flux changes according to its characteristic pressure demand curve. Unique to flow boiling, during two-phase operation, the pressure demand of the channel can increase with reducing mass flux as the amount of vapor generation increases (higher exit vapor quality); bubbles accelerate the flow as they nucleate, grow, and become confined by the channel walls. If there is a source of compressibility upstream of the channel inlet, the system will dynamically respond to this demand increase, pressurizing the compressible volume and momentarily reducing mass flux into the channel. Eventually, the upstream compressible volume pressurizes enough to overcome the channel pressure drop and mass flux into the channel increases,

causing a temporary reduction in vapor quality within the channel. A periodic continuation of this cycle characterizes the pressure drop oscillation instability. In a parallel channel system, the two-phase mixture within neighboring channels can interact in a similar way, even without the presence of a compressible volume upstream of the channel inlets. In this case, individual channels experience vapor confinement, backflow, and rewetting, in cycles that are out of phase with neighboring channels.

Investigations of these dynamic two-phase flow instabilities, primarily in macro-scale channels, are documented in a number of reviews [10], [14]–[18]. Most of these studies focused on the fundamental two-phase flow dynamics and instability mechanisms under idealized conditions, with comparatively less attention directed at understanding the impact of pressure drop oscillations and parallel channel instabilities on heat transfer performance in practical heat sink geometries. Of those that do studied practical heat sink geometries, the focus was on suppressing instabilities through methods such as inlet restrictors [19]–[21], rather than quantifying the heat transfer implications of the instabilities. Our recent study [22] reported on the development of a novel two-phase flow facility that could isolate and identify the effects of pressure drop oscillations on surface temperature and critical heat flux in single channels. This was achieved by comparing time-averaged surface temperatures and transient pressure signals in a single 20 mm long square-cross-section microchannel (w_c = 0.5, 0.75, and 1 mm) with and without the presence of an upstream compressible volume. The presence of the compressible volume was found to induce pressure drop oscillations with frequencies that increased in a range from $10 - 40$ Hz with increasing heat flux, similar to the frequencies reported by Kingston *et al.* [23] for a single 0.5 mm-diameter glass microchannel. These pressure drop oscillations resulted in an increase in time-averaged surface temperatures ranging from $0.5 - 6.0$ °C. The severity of the temperature rise was found to directly correlate with both the amplitude and frequency of the pressure drop oscillations, and performance was more sensitive to the oscillations in smaller channel geometries. The critical heat flux was insensitive to the occurrence of pressure drop oscillations except in the smallest channel geometry of w_c = 0.5 mm.

The current study is the first to delineate the individual and combined effects of both pressure drop oscillations and parallel channel instabilities on the heat transfer performance in parallel channel systems. Using the two-phase flow loop developed in our previous work [22], coupled with a modified parallel microchannel heat sink test section, the effect of these instabilities on surface temperature and critical heat flux is investigated. The coolant, material properties, and geometry of the heat sinks are informed by emerging two-phase cold plate applications. The heat sinks have square-cross-section channels ranging from w_c of 0.25 mm to 1 mm machined into a copper block and are tested over a range of mass fluxes

(100, 400, and 1600 kg/m^{2}s) under multiple flow configurations designed to isolate parallel channel instabilities from pressure drop oscillations relative to a baseline case with stable flow. The occurrence and type of the dynamic instabilities are identified through analysis of high-frequency pressure measurements synchronized with high-speed visualizations. The impact of these instabilities on heat transfer performance is assessed through comparison of time-averaged heat transfer results across the different flow configurations.

2 Experimental Methods

2.1 Flow Configurations

Three different flow configurations, shown schematically in Fig. 1, are employed to investigate the effect of pressure drop oscillations and parallel channel instabilities on heat transfer performance of a parallel channel heat sink. First, baseline stable flow boiling conditions are provided by configuration (i), where flow restrictors are installed at the inlet of each individual channel in the heat sink. Such inlet restrictors are an established method for preventing interaction between the two-phase mixture in the channels with either neighboring channels or compressibility in the system upstream of the heat sink [24]. For the second configuration (ii), the channel inlet restrictors are removed. This provides the necessary conditions for parallel channel instabilities to occur by allowing neighboring channels to interact with one another. However, because no upstream compressible volume is present in this configuration, pressure drop oscillations will not occur. In the final configuration (iii), an upstream compressible volume is added and the channel inlet restrictors are removed, providing conditions that allow for both pressure drop oscillations and parallel channel instabilities to occur. The specific experimental methods used to implement these three flow configurations are described in Section 2.2 below.

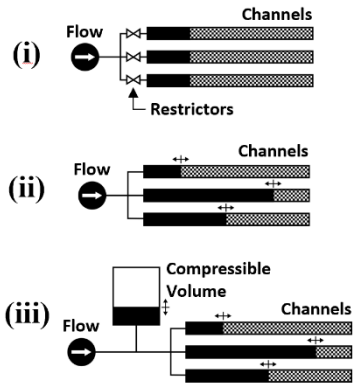

Fig. 1. Schematic diagrams of the three flow configurations implemented: (i) with inlet restrictors; (ii) without inlet restrictors; and (iii) with an upstream compressible volume. Shaded regions differentiate the length of the channels filled with two-phase mixture from the solid black regions filled with liquid only. The interface between these regions can move upstream or downstream during instabilities.

2.2 Flow Loop and Test Section

The experimental two-phase flow facility used in this study, shown schematically in Fig. 2, is charged with the dielectric fluid HFE-7100 [25]. For degassing of the working fluid, the custom-built reservoir is equipped with immersion heaters and Graham condensers connected to a chilled water supply. The reservoir remains open to atmosphere through the Graham condensers throughout all tests. A positive displacement gear pump (GB-P23, Micropump) provides the desired flow rate through the system. Fine control of liquid flow rate to the test section is achieved by regulating a portion of the flow through a bypass at the pump exit leading back to the reservoir. After the remaining fluid flow passes through an activated carbon filter and 7 μm particulate filter, the mass flow rate is measured by a Coriolis mass flowmeter (Micromotion CMF010M). The liquid temperature is either reduced using a liquid-to-air heat exchanger or increased by applying power to the electrically heated liquid preheater to achieve the desired inlet subcooling before it enters the test section.

The flow loop differs from the description in Ref. [22] in two primary ways to adapt the facility to the order-of-magnitude higher flow rates required for the parallel-channel experiments compared to a single channel. First, a needle valve that was located between the buffer volume and the test section is removed to prevent a large flow resistance across the valve, even when fully opened, from undesirably damping interaction between the test section and the buffer volume. Second, an additional heat exchanger is added between the flow meter and preheater to aid in maintaining the desired inlet subcooling to the heat sink. All other components and sensor arrangements are identical.

Any of the components within the flow loop might contain trapped air despite thorough degassing of the working fluid prior to and during each experiment. This trapped air can provide a source of upstream compressibility which can interact with the test section and induce pressure drop oscillations during flow configurations in which it is to be avoided. The needle valve labeled “system throttle” in Fig. 2 is used to maintain a system pressure, defined just upstream of the valve, of at least 90 kPa above the outlet pressure in the test section. This system pressure is approximately an order of magnitude greater than the nominal pressure drop across the test section and thereby effectively suppresses any interaction between a two-phase mixture in the test section and compressibility in the components upstream.

In order to allow for a controlled degree of compressibility upstream of the heat sink inlet, a custom-fabricated graduated glass cylinder (labeled “buffer volume” in Fig. 2) with threaded connections on either end is situated between the system throttle and the test section inlet. Under the flow configuration where an upstream compressible volume is desired, the cap on top of the buffer volume is removed and the valve labeled “buffer cut-off” in Fig. 2 is opened while circulating the working fluid, allowing the liquid level within the buffer to rise to a specified level. The buffer cut-off valve is then closed and the buffer volume capped, trapping a measurable volume of air at atmospheric pressure within the glass cylinder. At the beginning of the experiment, the buffer cut-off valve is opened, exposing the volume of compressible air to the test section inlet. A float ball placed in the cylinder minimizes the liquid-air interfacial area and prevents the air from dissolving into the working fluid. For flow configurations where zero upstream compressible volume is desired, the buffer cut-off valve remains closed.

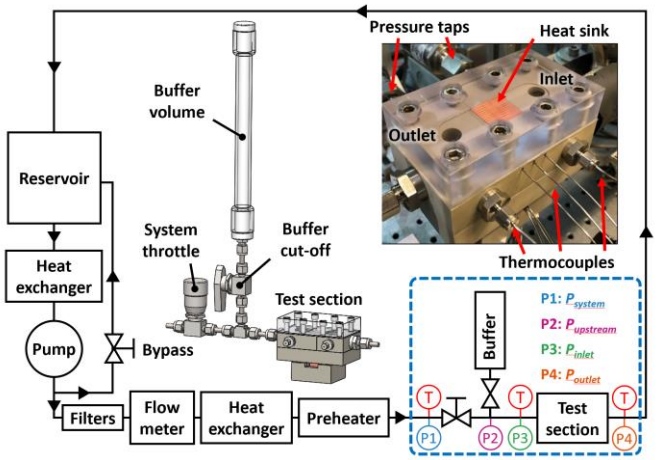

Fig. 2. Schematic diagram of the flow loop including an inset 3D model of the test section and buffer volume outlined in the blue dashed region of the flow loop. A labelled photograph of the instrumented parallel microchannel test section is also shown.

The test section assembly detailed in Fig. 3 is a modified version of that used in Ref. [22]. The component labeled "heat sink" in the cross-section view of the assembly in Fig. 3(a) is an interchangeable 20 mm × 20 mm × 10 mm oxygen-free copper block with microchannels directly machined into the top surface. For this study, four different parallel microchannel heat sink geometries are machined using a series of circular jeweler saw blades and spacers installed onto a custom mandril. The heat sinks include three thermocouple taps located 2.5 mm below the top surface and reaching into the centerline of the block at the inlet, center, and outlet of the channels. Heat is supplied through resistance cartridge heaters inserted into the bottom of a separate copper block below the heat sink. A thermal interface material (Laird Technologies, Tflex 700) is placed between the heater block and heat sink. The particular thermal interface material is chosen because it has a low dependence of thermal resistance on contact pressures above 70 kPa, thereby providing good test-to-test repeatability as it is also replaced each time a new heat sink is installed in the test section. The heat sink is held in alignment with the surrounding PEEK (polyether ether ketone) carrier by steel alignment pins as shown in the exploded assembly view in Fig. 3(b). Fluid is routed through manifolds machined into the PEEK carriers, which include taps for temperature and pressure measurements at the inlet and outlet plenums as labeled in Fig. 3(a).

For flow configuration (i) with channel inlet restrictions, restrictor plates are laser-cut (Universal Laser Systems, PLS6MW) from 3.2 mm-thick PTFE and aligned using the existing steel alignment pins as shown in Fig. 3(b). Each individual restrictor orifice is aligned to the center of the corresponding microchannel inlet. The nominal restrictor designs are circular in shape with nominal diameters of 0.21, 0.3, and 0.4 mm for the w_c = 0.5, 0.75, and 1 mm channels, respectively. Restrictors for the w_c = 0.25 mm channels could not be fabricated due to limitations on the minimum hole diameter that could be laser-cut in the PTFE plate. The nominal restrictor diameters correspond to a fixed restrictor-to-channel area ratio of 16%, which was chosen based on modeling results for the restrictor ratio required to suppress static instabilities [26], [27]. The laser-cutting process produces a hole that is conical in shape, where the diameter of the hole at the narrow end of the cone is close to the nominal diameter; the small end of the cone is positioned facing towards the heat sink. Unintended flash boiling of the fluid due to expansion after the restrictor was of concern, but this was not observed during testing with restrictors. Additional details regarding the test section assembly and sealing method can be found in Ref. [22].

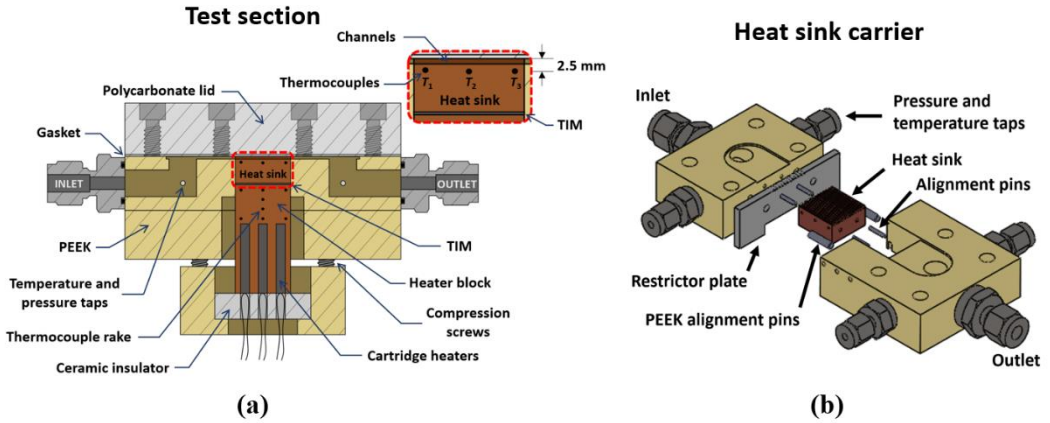

Fig. 3. (a) Cross-sectional view of the test section with identification of key components and (b) exploded view of the heat sink carrier assembly with a restrictor plate installed.

2.3 Experimental Procedure

Experiments are performed using four parallel microchannel heat sinks, each with different channel cross section dimensions, as listed in Table 1. The nominal channel sizes were chosen to match those of the previous single-channel study [22] (w_c = 0.5, 0.75, and 1 mm) with an additional smaller channel size of w_c = 0.25 mm. The nominal wall thickness is equal to the channel width except for the 0.25 mm channels, where the wall thickness is 0.5 mm to maintain structural rigidity during machining. The wall thicknesses were chosen to ensure a fin efficiency greater than 97%. All heat sinks have a flow length of 20 mm. The actual as-fabricated channel dimensions were measured under a microscope (Olympus BX53M), and the mean channel widths and heights are listed in Table 1. Each heat sink is tested over the range of mass fluxes listed in Table 2 under the three flow configurations described in Section 2.1, with the exception of the heat sink with w_c = 0.25 mm channels, which is not tested with inlet restrictors. The working fluid is degassed for a minimum of 2 hr prior to the start of each experiment by vigorously boiling the fluid in the reservoir while allowing noncondensable gasses to vent out of the system through the Graham condensers and circulating the fluid through the facility. This process ensures that any air trapped within the test section or other components is dissolved into the working fluid flowing through the lines and then expelled from the system through the Graham condensers. By maintaining saturated boiling conditions in the reservoir throughout the experiments, the working fluid is held in a degassed state.

At the beginning of each experiment, the desired inlet subcooling, mass flux, and flow configuration are set while maintaining a system pressure of 90-100 kPa above the outlet pressure. The inlet subcooling is set at 20 °C as measured by the thermocouple in the test section inlet plenum. For each flow configuration, power supplied to the heater is incremented in small steps, allowing a steady state to be reached at each step where data is recorded as described in Section 2.4. A complete boiling curve of the measured heat flux versus surface superheat is thereby constructed that spans flow regimes from single-phase to two-phase operation, up to the critical heat flux (CHF). This procedure is repeated for each heat sink and mass flux combination listed in Table 2 under flow configurations (i) with inlet restrictors, (ii) without inlet restrictors, and (iii) with a compressible volume and no inlet restrictors.

Table 1. Measured heat sink channel dimensions.

Number of Channels, N	Mean Channel Width, w_c [mm]	Mean Channel Height, h_c [mm]
26	0.29	0.29
19	0.55	0.47
12	0.85	0.83
10	1.04	0.99

Table 2. Nominal test parameters.

Number of Channels, N	Channel Width, w_c [mm]	Mass Flux, G [kg/m^{2}s]	Flow Rate, $\dot{V}$ [mL/min]	Heat Flux, q'' [W/cm^2]
26	0.25	100	7	0 – 8
		400	26	0 – 25
		1600	105	0 – 59
19	0.5	100	19	0 – 12
		400	77	0 – 34
		1600	308	0 – 60
12	0.75	100	27	0 – 14
		400	110	0 – 36
		1600	438	0 – 64
10	1	100	41	0 – 10
		400	162	0 – 23

2.4 Data Acquisition and Processing

A data acquisition system (National Instruments cRIO-9024) with the necessary input/output modules is used to record data from all sensors in the facility. In order to capture transient pressure fluctuations associated with dynamic two-phase flow instabilities, high-frequency characterization is required [23]. Pressure transducers are sampled at a frequency of 25 kHz and down-sampled by averaging every 10 data points to reduce noise. These high-frequency pressure signals are paired with high-speed visualizations (Vision Research, Phantom v1212), which are sampled at 1000 frames per second and triggered simultaneously by the data acquisition system. The test section is illuminated by an LED panel (Advanced Illumination). At each steady-state heat flux, 10 s of high-frequency pressure data and high-speed video are recorded. All other data are sampled over 2 min at a rate of 1 Hz and time-averaged. Pressure transducers are calibrated (Scandura, Pascal 100) prior to experimentation.

Heat loss from the heater block, Q_{loss}, is experimentally calibrated as described in Ref. [22]. Heat flux within the heater block is calculated by subtracting Q_{loss} from the total electrical power, P_{elec}, supplied to the cartridge heaters. The total electrical power is calculated from the voltage drop across the power supply and the electrical current measured using a shunt resistor. Channel wetted-area heat flux is calculated assuming that the power supplied to the heat sink is equal to the heat-loss-corrected power supplied to the heater block ($q'' = (P_{elec} - Q_{loss})/A_{wet}$). Channel surface temperatures are extrapolated from the three thermocouples embedded along the centerline of the heat sink 2.5 mm below the top surface using the channel wetted-area heat flux. Sensor measurement uncertainties as well as uncertainties in the wetted-area heat flux and extrapolated surface temperature are calculated as described in Ref. [22] and listed in Table 3.

Table 3. Summary of measurement uncertainties.

Measurement	Uncertainty
Calibrated T-type thermocouples	$\pm$0.3 °C
Pressure transducers	$\pm$2.13 kPa
Wetted-area heat flux	$\pm$0.02 W/cm^2 (lowest flux) to $\pm$0.2 W/cm^2 (highest flux)
Extrapolated surface temperature	$\pm$0.4 °C

3 Results and Discussion

Time-averaged heat transfer data are presented and compared for thermal performance across all test parameters and flow conditions. Trends associated with the time-averaged data are then explained using high-frequency pressure data and flow visualizations.

3.1 Time-Averaged Flow Boiling Behavior

Time-averaged steady-state boiling curves for all test cases in Table 2 are presented in Fig. 4. The boiling curves present the channel wetted-area heat flux plotted against the difference between the time-averaged channel surface temperature and the saturation temperature of the fluid at atmospheric pressure, also known as surface superheat. Channel surface temperature is the mean value of the three thermocouples positioned along the channel length. Each subplot in Fig. 4(a-d) corresponds to a particular channel size and the individual curves correspond to different mass fluxes grouped by color. For each mass flux, the shape of the data point denotes the flow configuration: (i) triangles correspond to tests with inlet restrictors installed; (ii) squares correspond to tests without inlet restrictors; and (iii) circles correspond to tests without inlet restrictors and a compressible volume upstream of the heat sink inlet.

All of the individual boiling curves follow a common characteristic trend. At the lowest heat fluxes, the surface superheat increases linearly with heat flux as the heat sink operates in the single-phase regime, reflecting the expected constant heat transfer coefficient for single-phase internal flow. For the same channel size and mass flux, the surface superheat for configuration (i) is lower than for configurations (ii) and (iii) for a given heat flux within the single-phase regime. This decrease in temperature is attributed to expansion of flow exiting the channel inlet restrictors. Once nucleate boiling begins in the heat sink, the boiling curves turn sharply upward reflecting the increased heat transfer coefficient associated with phase change. Within this two-phase flow regime, the curves collapse indicating that the heat transfer coefficient is independent of mass flux. The heat sink operates within this regime with increasing heat flux until a critical heat flux condition is reached, which is indicated by an immediate transient excursion in channel surface temperature and visual observation of local dryout within channels in the heat sink. The data point at the highest heat flux for each individual boiling curve presented in Fig. 4 corresponds to the final steady-state data recorded prior to the occurrence of CHF. This final steady-state value is chosen to represent CHF in the discussion below.

In the w_c = 0.25 mm heat sink (Fig. 4(a)), boiling curves corresponding to flow configurations (ii) and (iii), with their potential for flow instabilities in the absence of inlet restrictors, generally overlap within the two-phase flow region across all mass fluxes. In terms of surface superheat, the difference between these two flow configurations is negligible. The boiling curves primarily differ in their CHF limit, which

depends heavily on mass flux, increasing from 7.9 W/cm^2 at the lowest (G = 100 kg/m^{2}s) to 58.7 W/cm^2 at the highest (G = 1600 kg/m^{2}s) mass fluxes for flow configuration (ii). The addition of an upstream compressible volume in configuration (iii) leads to a slight reduction in CHF of 4 W/cm^2 or less; this effect is minor compared to the CHF sensitivity to mass flux.

Similar observations are made in Fig. 4(b) for all three flow configurations with the next larger channel size (w_c = 0.5 mm). In the nucleate boiling regime, the curves spanning all three mass fluxes and flow configurations overlap, indicating that the effect of the flow configurations has minor impact on heat sink surface temperature, with any differences being within the limits of measurement uncertainty. The CHF is seen to be insensitive to the different flow configurations, with any small differences in CHF falling within the span of a single steady-state power increment. As in the case of the smallest channel size, CHF is sensitive to mass flux, increasing by approximately 5.5 times as the mass flux increases from G = 100 kg/m^{2}s to G = 1600 kg/m^{2}s.

A greater influence of flow configuration on surface superheat is observed at the next larger channel size, w_c = 0.75 mm (Fig. 4(c)). At the lower mass fluxes of G = 100 and G = 400 kg/m^{2}s, a surface temperature increase of up to 3 °C is observed when the inlet restrictors are removed (from configuration (i) to (ii)), while a further increase of 3 °C results upon the inclusion of an upstream compressible volume in configuration (iii). No significant variation in surface temperature between flow configurations is observed at the highest mass flux of G = 1600 kg/m^{2}s; as will be discussed in the coming sections, flow instabilities are suppressed at this highest mass flux. At the lower mass fluxes of G = 100 and G = 400 kg/m^{2}s, the CHF is largely insensitive to flow configuration (with minor changes being within a single power-increment span). However, at the highest mass flux of G = 1600 kg/m^{2}s, a significant reduction of approximately 12.5 W/cm^2 in CHF was observed for configuration (iii) with an upstream compressible volume compared configurations (i) and (ii). In this outlier case, no instabilities were observed until the final increment in heat flux, whereupon instabilities were triggered and resulted in immediate occurrence of CHF. This is attributed to the stochastic nature of these boiling processes, and the authors expect that, if this test were repeated many times, the CHF would be extended to higher heat fluxes in some cases.

The heat sink with the largest channel w_c = 1 mm (Fig. 4(d)) generally exhibits higher surface temperatures at a given heat flux relative to the smaller channel geometries. Like the w_c = 0.75 mm heat sink, a small increase in surface temperature is observed operating under configuration (iii) with a compressible volume compared to configuration (i) with inlet restrictors at the two mass fluxes tested. Configuration (ii) without the compressible volume, however, resulted in little to no increase in surface

temperature relative to the case with inlet restrictors. No significant change in CHF is observed at either mass flux across the three flow configurations.

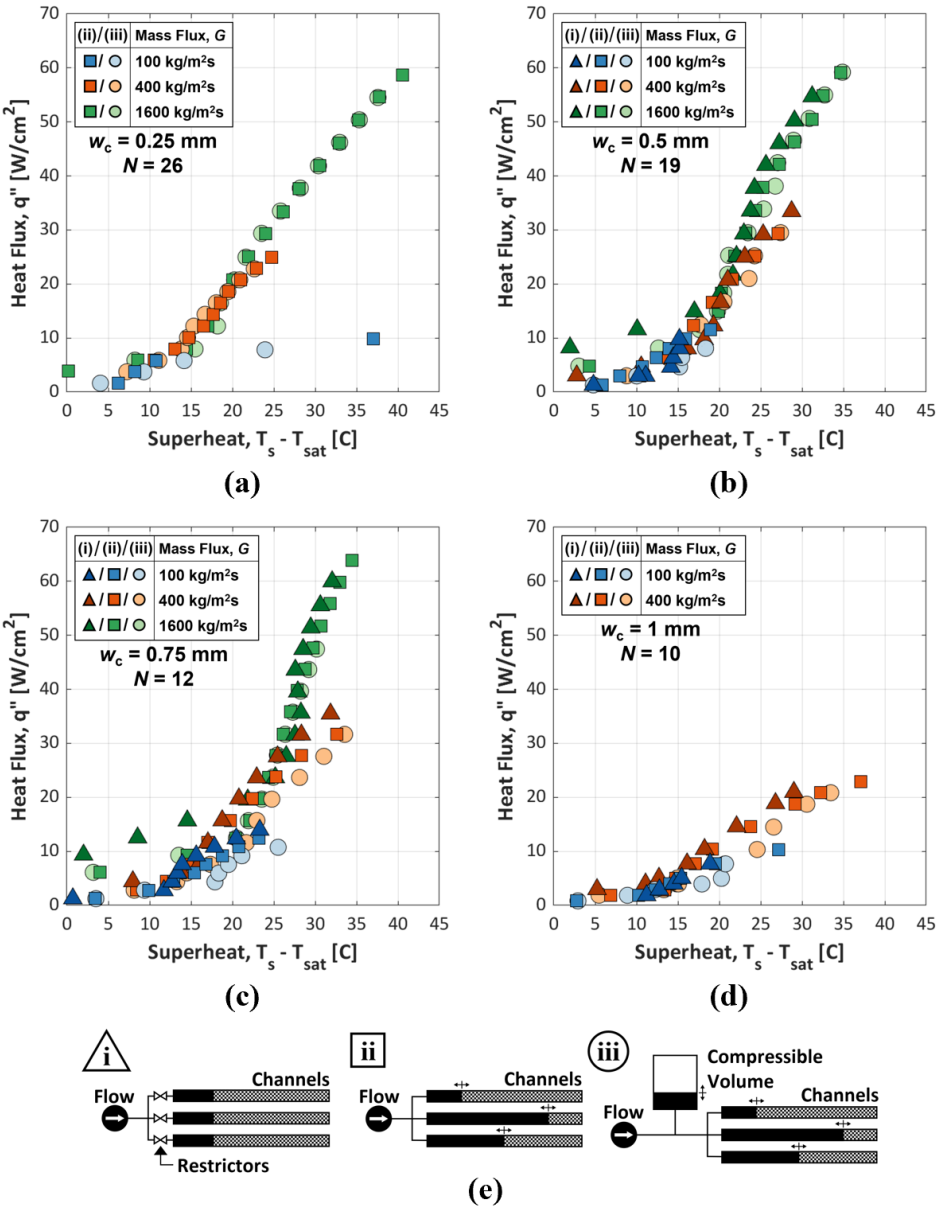

Fig. 4. Boiling curves at mass fluxes of 100, 400, and 1600 kg/m^{2}s for the four microchannel heat sink geometries: (a) N = 26, w_c = 0.25 mm; (b) N = 19, w_c = 0.5 mm; (c) N = 12, w_c = 0.75 mm; (d) N = 10, w_c = 1 mm. The symbols used to plot the curves corresponds to the (e) different flow configurations: (i) with inlet restrictors, (ii) without inlet restrictors, and (iii) with an upstream compressible volume.

3.2 Transient Two-Phase Flow Pattern Observations

Although the time-averaged surface temperature and CHF limit were found to be generally insensitive to the flow configuration, as discussed in Section 3.1, each configuration is characterized by quite different transient two-phase flow patterns as observed via high-speed visualization and high-frequency pressure measurements. In Fig. 5, still-frame images from these visualizations are selected to best showcase the nature of these flow patterns under each flow configuration for the w_c = 0.75 mm heat sink at G = 400 kg/m^{2}s and q'' = 20 W/cm^2. This operating condition had the most contrast between the different flow configurations of all the time-averaged heat transfer data. Under each annotated frame, the transient pressure data $\hat{P}_{inlet} = P_{inlet} - P_{inlet,mean}$ is plotted over a 10 s duration and the time of the still frame is marked as a dashed, vertical red line.

Flow configuration (i) is shown in Fig. 5(a) where the individual restrictor orifices are outlined with horizontal dashed lines at the inlet of the heat sink. After the subcooled liquid passes through the restrictor orifice and enters a channel, there is a short length over which the bulk fluid remains as a single-phase liquid. Further downstream, nucleate boiling is initiated and the bubbles generated depart and exit the channel downstream with no signs of flow reversal. The dashed blue line serves as a visual aid to mark the approximate location within each channel where boiling begins. The location of this single-to-two-phase transition is steady in time and the two-phase flow is thereby determined to be stable. This is reflected in the corresponding plot where $\hat{P}_{inlet}$ remains constant across the 10 s recording window and only negligible fluctuations are observed.

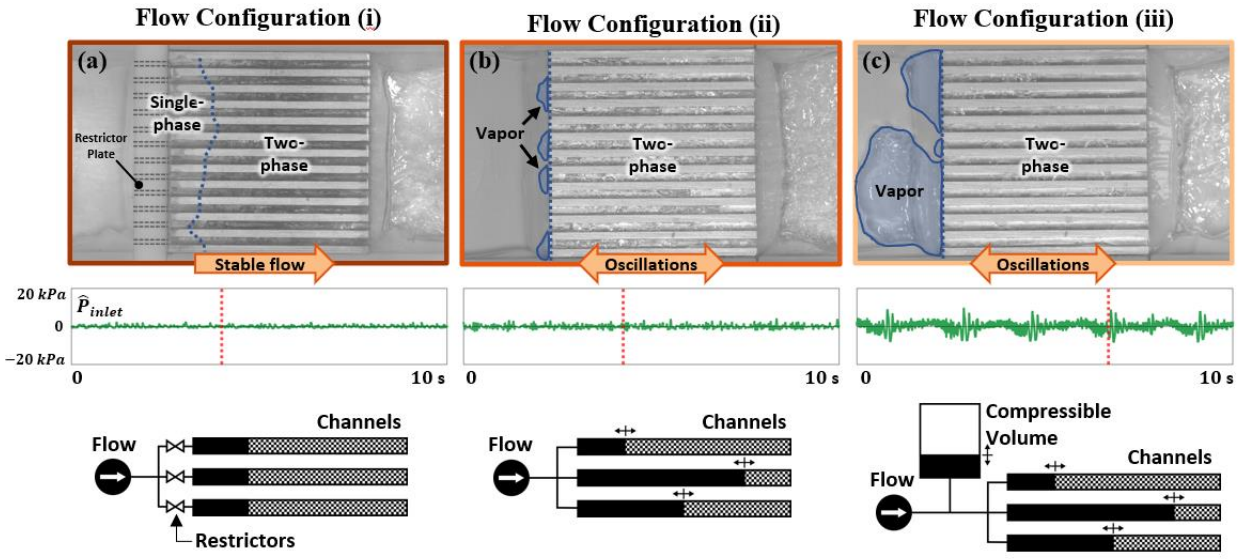

Fig. 5. Snapshots of the N = 12, w_c = 0.75 mm heat sink at a mass flux of 400 kg/m^{2}s and heat flux of 20 W/cm^2 for flow configurations (a) with inlet restrictors, (b) without inlet restrictors, and (c) with an upstream compressible volume. Below each snapshot, $\hat{P}_{inlet} = P_{inlet} - P_{inlet,mean}$ is plotted over 10 s and the location of the snapshot frame is noted by a vertical dashed, red line. See Electronic Annex 1 in the online version of this article for full length videos.

An image frame from flow configuration (ii) with the inlet restrictors removed is shown in Fig. 5(b). Under this configuration, the two-phase mixture in an individual channel can dynamically interact with the mixture in neighboring channels. In the case shown in Fig. 5(b), this results in the occurrence of parallel channel instabilities. During this instability, vapor generated within an individual channel becomes confined and, due to the compressibility in neighboring channels, bubble growth is permitted in both upstream and downstream directions. Vapor from the channel is ejected into the inlet header and either condensed by the incoming subcooled liquid or is driven into neighboring channels until eventually subcooled liquid enters the channel again. In the chosen frame representing this flow pattern, vapor pockets which have been ejected into the inlet header from individual channels are filled in blue and labeled. Unlike configuration (i) in Fig. 5(a), there is no stable boiling regime established in any of the channels throughout the heat sink and the dashed line indicating the start of the two-phase region is drawn vertically at the inlet. Because the inlet pressure is measured across the array of channels within the inlet plenum, flow oscillations localized to individual channels and at different phases register in the pressure data as only a small amount of additional noise in $\hat{P}_{inlet}$, as plotted below the still frame.

The final flow configuration (iii) is shown in Fig. 5(c), where inlet restrictors are removed, and the test section is allowed to interact with a compressible volume located in the upstream buffer. Like configuration (ii), the individual channels can interact with one another, and parallel channel instabilities are observed to occur. However, the presence of the compressible volume upstream of the heat sink also provides the conditions necessary for pressure drop oscillations, resulting in a co-existence of the two types of dynamic instabilities. The pressure drop oscillations are observed to act on a heat-sink-level, as opposed to parallel channel instabilities which act on individual channels. For the heat sink geometry and operating conditions shown in Fig. 5, pressure drop oscillations appear as lower frequency oscillations occurring across the entire heat sink width, where vapor confinement and flow reversal occurs in unison across all channels and the combined vapor ejected from the channels spans the entire heat sink, as outlined in Fig. 5(c) as the blue regions. Once the pressure in the buffer increases enough to overcome the momentary increase in the heat sink pressure drop, all channels are flooded again with subcooled fluid. This is typically followed by secondary oscillations throughout all channels of a higher frequency, as can be seen in $\hat{P}_{inlet}$ plotted in Fig. 5(c). During the portion of the pressure drop oscillation cycle where backflow is not occurring on a heat-sink-level, flow through individual channels is still observed to oscillate at a high frequency indicative of parallel channel instabilities. In general, the amplitude of heat-sink-level oscillations is observed to increase, and the frequency is observed to decrease, with increasing channel width. This is likely resulting in the apparent increase in the effect of instabilities on time-averaged surface temperatures for larger channel geometries in Fig. 4.

3.3 Effect of Mass Flux

To demonstrate the effect of mass flux on the occurrence of dynamic instabilities, it is useful to compare cases at a constant boiling number, which represents the ratio between the applied heat flux and the theoretical heat flux required to vaporize all of the fluid, $Bl = q''/(Gh_{fg})$. A constant Boiling Number implies that the exit vapor quality is the same across each case. Fig. 6 shows still-frame images and pressure signals for the w_c = 0.75 mm heat sink under flow configuration (iii) at mass fluxes of 100, 400, and 1600 kg/m^{2}s at a constant Bl = 0.0024, corresponding to heat fluxes of 3, 12, and 47 W/cm^2, respectively. At the lowest mass flux G = 100 kg/m^{2}s (Fig. 6(a)), heat-sink-level oscillations resulting in vapor backflow spanning all channels into the plenum are observed at a regular frequency. At this heat flux, pressure drop oscillations dominate the flow pattern, appearing as periodic oscillations at a single frequency in the pressure signal; parallel channel instabilities are not observed. At the intermediate mass

flux G = 400 kg/m^{2}s (Fig. 6(b)), the flow in the channels again oscillates in unison due to the interaction with the upstream compressible volume, though this oscillation appears as a less defined frequency in the pressure signal, due to some out-of-phase channel-to-channel oscillations associated with parallel channel instabilities. At the highest mass flux G = 1600 kg/m^{2}s (Fig. 6(c)), the flow inertia is sufficient to suppress both pressure drop oscillations and parallel channel instabilities and no backflow is observed in the visualizations. Instead, the flow pattern appears similar to that observed in flow configuration (i) with inlet restrictors, where the subcooled fluid remains in single-phase over a short distance before nucleation begins at a stable streamwise location in the channel.

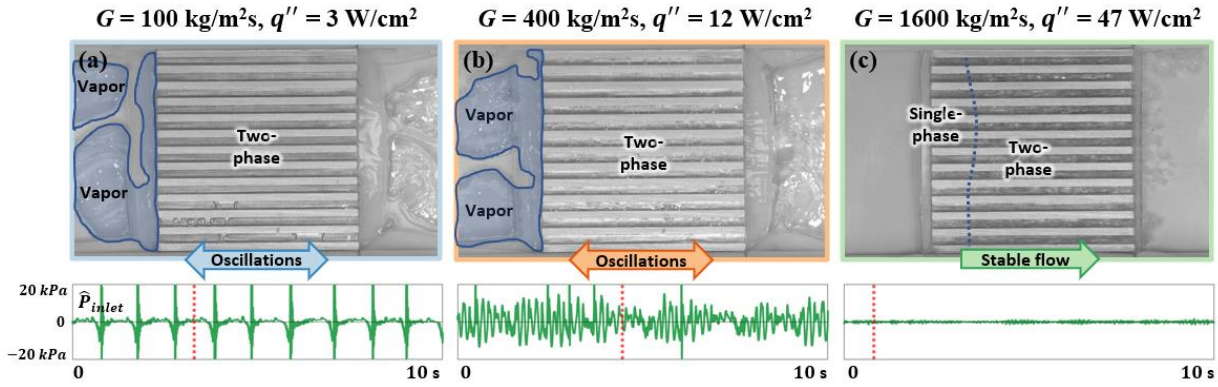

Fig. 6. Snapshots of the N = 12, w_c = 0.75 mm heat sink at mass fluxes of (a) 100 kg/m^{2}s, (b) 400 kg/m^{2}s, and (c) 1600 kg/m^{2}s for flow configuration (iii) with an upstream compressible volume, where snapshot boxes are colored to correspond with boiling curves above. Below each snapshot, $\hat{P}_{inlet} = P_{inlet} - P_{inlet,mean}$ is plotted over 10 s and the location of the snapshot frame is noted by a vertical dashed, red line. See Electronic Annex 2 in the online version of this article for full length videos.

3.4 Wall Temperature Fluctuations

When pressure drop oscillations occur under flow configuration (iii) with an upstream compressible volume and cause heat-sink-level oscillations in mass flux, corresponding oscillations in surface temperatures are also observed. To showcase an example, temperature signals corresponding to the three thermocouples embedded 2.5 mm below the top surface of the w_c = 0.75 mm heat sink are plotted in Fig. 7 over a 60 s duration at a mass flux of G = 400 kg/m^{2}s and heat flux of 28 W/cm^2 under each flow configuration. Temperatures T_1, T_2, and T_3 correspond to the thermocouples located 2, 10, and 18 mm respectively from the inlet along the centerline of the heat sink. Under flow configuration (i), the temperature signals (Fig. 7(a)) remain constant and no oscillations are observed due to the stable flow pattern produced by the inlet restrictors. When parallel channel instabilities are present under flow configuration (ii) due to the removal of the inlet restrictors, oscillations occur within individual channels

throughout the heat sink, with these oscillations being out of phase with one another. Due to effective heat spreading in the thick copper heat sink base, these channel-level follow oscillations do not result in any oscillations in the temperature signals (Fig. 7(b)). However, the mean temperatures are higher than those observed under configuration (i), as discussed in the analysis of the time-averaged data in Section 3.1. In contrast, the heat-sink-level mass flux oscillations caused by pressure drop oscillations under flow configuration (iii) result in a measurable oscillation of the temperature at each thermocouple location, as seen in Fig. 7(c). In this example, the oscillation occurs at a frequency of approximately 0.24 Hz, which is similar to the frequency of pressure drop oscillations observed in the pressure signal. Across the three thermocouples, the maximum peak-to-trough fluctuation is 2.6 °C. Given that the penetration depth ($\delta_p = 4\sqrt{2\pi\alpha/f}$) at this frequency is 34 mm into the copper block, the amplitude of the temperature fluctuation at the surface is not expected to differ from that measured at the embedded thermocouple depth.

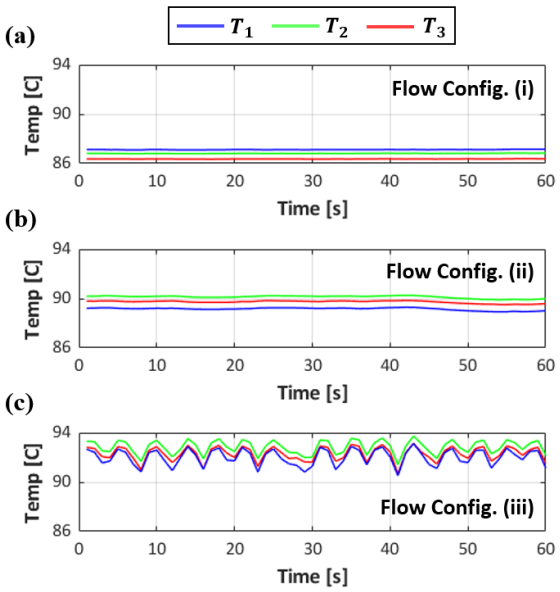

Fig. 7. Temperature signals of thermocouples embedded 2.5 mm below the top surface of the N = 12, w_c = 0.75 mm heat sink at G = 400 kg/m^{2}s and q'' = 28 W/cm^2 for flow configurations (a) with inlet restrictors, (b) without inlet restrictors, and (c) with an upstream compressible volume.

4 Conclusions

Flow boiling experiments were performed in parallel microchannel heat sinks of four different channel sizes (w_c = 0.25 mm, 0.5 mm, 0.75 mm, and 1 mm) at mass fluxes of 100, 400, and 1600 kg/m^{2}s

under three flow configurations to isolate and investigate the effects of pressure drop oscillations and parallel channel instabilities. Configuration (i) with flow restrictors at the inlet to each individual channel in the heat sink provides a stable flow boiling condition. Configuration (ii) removes these inlet restrictors to provide conditions where parallel channel instabilities can occur. Configuration (iii) with a compressible volume added upstream provides conditions necessary for both parallel channel instabilities and pressure drop oscillations to occur. By comparing the time-averaged heat transfer performance and transient flow patterns produced by these three flow configurations, the following conclusions are drawn regarding the impact of pressure drop oscillations and parallel channel instabilities:

- Across the range of geometries and flow conditions tested, time-averaged surface temperatures are generally insensitive to the occurrence of the dynamic instabilities, and the boiling curves corresponding to the three flow configurations nearly overlap. In a few exceptions, such as the w_c = 0.75 mm heat sink, a modest temperature rise due to the presence of instabilities is observed, with a maximum increase of approximately 6 °C.
- The effect of both parallel channel instabilities and pressure drop oscillations on the critical heat flux (CHF) is small. Any differences observed were within a single 4 W/cm^2 steady-state power increment used in the current experiments. One exception is a significant reduction in CHF of 12.5 W/cm^2 in the w_c = 0.75 mm heat sink at a mass flux of G = 1600 kg/m^{2}s under the flow configuration with an upstream compressible volume.
- When pressure drop oscillations result in heat-sink-level mass flux oscillations, transient fluctuations in temperatures are also observed. The maximum amplitude of such temperature fluctuations observed across all tests is approximately 3 °C. During both stable flow boiling and the occurrence of parallel channel instabilities, no fluctuations are observed in measured temperatures.
- While mass flux oscillations resulting from pressure drop oscillations and parallel channel instabilities might have greater effect under some conditions, the impact on time-averaged surface temperatures and critical heat flux is generally small in the system studied in this work. Further study is warranted into the effects of heat sink thermal capacity, which may impact the transient temperature response during oscillations in mass flux and represent a critical system parameter that governs whether these instabilities have deleterious effects.

Acknowledgements

This material is based upon work supported by Ford Motor Company through the Ford – Purdue University Alliance program. Special thanks to Dr. Edward Jih at Ford Research & Advanced Engineering (R&AE) for technical discussions related to this work.

References

[1] A. Bar-Cohen, M. Arik, and M. Ohadi, "Direct Liquid Cooling of High Flux Micro and Nano Electronic Components," *Proc. IEEE*, vol. 94, no. 8, pp. 1549–1570, 2006, doi: 10.1109/JPROC.2006.879791.

[2] K. P. Bloschock and A. Bar-Cohen, "Advanced thermal management technologies for defense electronics," in *Defense Transformation and Net-Centric Systems 2012*, 2012, vol. 8405, p. 84050I. doi: 10.1117/12.924349.

[3] M. Drinkwine, "DARPA's Intra/Interchip Enhanced Cooling (ICECool) Program," p. 4, 2013.

[4] A. Bar-Cohen, J. J. Maurer, and D. H. Altman, "Embedded cooling for wide bandgap power amplifiers: A review," *J. Electron. Packag.*, vol. 141, no. 4, 2019, doi: 10.1115/1.4043404.

[5] K. P. Drummond *et al.*, "Characterization of hierarchical manifold microchannel heat sink arrays under simultaneous background and hotspot heating conditions," *Int. J. Heat Mass Transf.*, vol. 126, pp. 1289–1301, 2018, doi: 10.1016/j.ijheatmasstransfer.2018.05.127.

[6] A. Bar-Cohen *et al.*, "The ICECool fundamentals effort on evaporative cooling of microelectronics," *IEEE Trans. Compon. Packag. Manuf. Technol.*, vol. 11, no. 10, pp. 1546–1564, 2021, doi: 10.1109/TCPMT.2021.3111114.

[7] R. K. Mandel, D. G. Bae, and M. M. Ohadi, "Embedded two-phase cooling of high flux electronics via press-fit and bonded FEEDS coolers," *J. Electron. Packag.*, vol. 140, no. 3, 2018, doi: 10.1115/1.4039264.

[8] J. A. Boure, A. E. Bergles, and L. S. Tong, "Review of two-phase flow instability," *Nucl. Eng. Des.*, vol. 25, no. 2, pp. 165–192, 1973, doi: 10.1016/0029-5493(73)90043-5.

[9] S. Kakac and B. Bon, "A Review of two-phase flow dynamic instabilities in tube boiling systems," *Int. J. Heat Mass Transf.*, vol. 51, no. 3, pp. 399–433, 2008, doi: 10.1016/j.ijheatmasstransfer.2007.09.026.

[10] Y. K. Prajapati and P. Bhandari, "Flow boiling instabilities in microchannels and their promising solutions – A review," *Exp. Therm. Fluid Sci.*, vol. 88, pp. 576–593, 2017, doi: 10.1016/j.expthermflusci.2017.07.014.

[11] A. Miglani, J. A. Weibel, and S. V. Garimella, "Measurement of flow maldistribution induced by the Ledinegg instability during boiling in thermally isolated parallel microchannels," *Int. J. Multiph. Flow*, vol. 139, p. 103644, 2021, doi: 10.1016/j.ijmultiphaseflow.2021.103644.

[12] T. A. Kingston, J. A. Weibel, and S. V. Garimella, "Ledinegg instability-induced temperature excursion between thermally isolated, heated parallel microchannels," *Int. J. Heat Mass Transf.*, vol. 132, pp. 550–556, 2019, doi: 10.1016/j.ijheatmasstransfer.2018.12.017.

[13] S. G. Kandlikar, *Handbook of Phase Change : Boiling and Condensation*, 1st ed. Boca Raton, FL, USA: CRC Press, 1999. doi: 10.1201/9780203752654.

[14] A. E. Bergles and S. G. Kandlikar, "On the nature of critical heat flux in microchannels," *J. Heat Transf.*, vol. 127, no. 1, p. 101, 2005, doi: 10.1115/1.1839587.

[15] J. R. Thome, "State-of-the-art overview of boiling and two-phase flows in microchannels," *Heat Transf. Eng.*, vol. 27, no. 9, pp. 4–19, 2006, doi: 10.1080/01457630600845481.

[16] S. G. Kandlikar, "History, advances, and challenges in liquid flow and flow boiling heat transfer in microchannels: A critical review," *J. Heat Transf.*, vol. 134, no. 3, pp. 034001-034001–15, 2012, doi: 10.1115/1.4005126.

[17] C. B. Tibiriçá and G. Ribatski, "Flow boiling in micro-scale channels – Synthesized literature review," *Int. J. Refrig.*, vol. 36, no. 2, pp. 301–324, 2013, doi: 10.1016/j.ijrefrig.2012.11.019.

[18] L. C. Ruspini, C. P. Marcel, and A. Clausse, "Two-phase flow instabilities: A review," *Int. J. Heat Mass Transf.*, vol. 71, pp. 521–548, 2014, doi: 10.1016/j.ijheatmasstransfer.2013.12.047.

[19] S. Szczukiewicz, N. Borhani, and J. R. Thome, “Two-phase flow operational maps for multi-microchannel evaporators,” *Int. J. Heat Fluid Flow*, vol. 42, pp. 176–189, 2013, doi: 10.1016/j.ijheatfluidflow.2013.03.006.
[20] G. Wang, P. Cheng, and A. E. Bergles, “Effects of inlet/outlet configurations on flow boiling instability in parallel microchannels,” *Int. J. Heat Mass Transf.*, vol. 51, no. 9, pp. 2267–2281, 2008, doi: 10.1016/j.ijheatmasstransfer.2007.08.027.
[21] S. G. Kandlikar, W. K. Kuan, D. A. Willistein, and J. Borrelli, “Stabilization of flow boiling in microchannels using pressure drop elements and fabricated nucleation sites,” *J. Heat Transf.*, vol. 128, no. 4, pp. 389–396, 2005, doi: 10.1115/1.2165208.
[22] M. D. Clark, J. A. Weibel, and S. V. Garimella, “Impact of pressure drop oscillations on surface temperature and critical heat flux during flow boiling in a microchannel,” *IEEE Trans. Compon. Packag. Manuf. Technol.*, pp. 1634–1644, 2021, doi: 10.1109/TCPMT.2021.3094767.
[23] T. A. Kingston, J. A. Weibel, and S. V. Garimella, “High-frequency thermal-fluidic characterization of dynamic microchannel flow boiling instabilities: Part 2 – Impact of operating conditions on instability type and severity,” *Int. J. Multiph. Flow*, 2018, doi: 10.1016/j.ijmultiphaseflow.2018.05.001.
[24] A. Koşar, C.-J. Kuo, and Y. Peles, “Suppression of boiling flow oscillations in parallel microchannels by inlet restrictors,” *J. Heat Transf.*, vol. 128, no. 3, pp. 251–260, 2006, doi: 10.1115/1.2150837.
[25] *3M Novec Engineered Fluid HFE-7100 for Heat Transfer*. St. Paul, MN, USA: 3M, 2002.
[26] T. Van Oevelen, J. A. Weibel, and S. V. Garimella, “Predicting two-phase flow distribution and stability in systems with many parallel heated channels,” *Int. J. Heat Mass Transf.*, vol. 107, pp. 557–571, 2017, doi: 10.1016/j.ijheatmasstransfer.2016.11.050.
[27] T. Van Oevelen, J. A. Weibel, and S. V. Garimella, “The effect of lateral thermal coupling between parallel microchannels on two-phase flow distribution,” *Int. J. Heat Mass Transf.*, vol. 124, pp. 769–781, 2018, doi: 10.1016/j.ijheatmasstransfer.2018.03.073.